# The use of neutron tomography for the structural analysis of corn kernels

T.E. Cleveland IV [a],[*],[1], D.S. Hussey [b], Z.-Y. Chen [c], D.L. Jacobson [b],
R.L. Brown [d], C. Carter-Wientjes [d], T.E. Cleveland [d], M. Arif [b],[**]

[a] *Tulane University, United States*
[b] *National Institute of Standards and Technology, Physics Laboratory, Ionizing Radiation Division, Neutron Interactions and Dosimetry Group,
100 Bureau Drive, Stop 8461, Gaithersburg, MD 20899-8461, United States*
[c] *Louisiana State University Agricultural Center, Department of Plant Pathology and Crop Physiology, Louisiana State University,
451 Life Sciences Building, Baton Rouge, LA 70894, United States*
[d] *U.S. Department of Agriculture, Agricultural Research Service, Southern Regional Research Center, Food and Feed Safety Unit,
1100 Robert E. Lee Boulevard, New Orleans, LA 70124, United States*

## Abstract

Neutron tomography was studied as a technique for non-destructively analyzing the internal structure of dried corn kernels. The study had two goals: first, to determine if the analysis could identify well-known anatomical features of the kernels; and second, to determine if it could distinguish between different types and treatments of kernels. Specifically, kernels which were infected vs. uninfected with the aflatoxin-producing fungus *Aspergillus flavus* were analyzed. Two different varieties of corn were used: VA35 (susceptible to *A. flavus* infection) and GT-MAS:gk (resistant). It was found that many anatomical features of the kernels could be identified using neutron tomography, including the scutellum, endosperm, aleurone, pericarp, pedicel, coleorhizae, radical, plumule, and coleoptile. Furthermore, differences were detected between susceptible kernels that had been inoculated and those that had not. Infected kernels were found to have lower neutron attenuation in the scutellum and embryo regions, possibly caused by lower hydrogen concentrations due to fungal degradation. No systematic structural differences were detected between resistant inoculated and resistant uninoculated kernels, as expected. This study indicated that neutron tomography could be a useful technique for the structural analysis of corn, and possibly other grains or small biological objects.
Published by Elsevier Ltd.

*Keywords:* Neutron radiography; Tomography; Corn structure; VA35; GT-MAS:gk; *Aspergillus flavus*

## 1. Introduction

Neutron imaging and tomography have been used to study the internal structure of many mechanical objects. Neutron imaging is conceptually similar to x-ray imaging, with the important difference that the attenuation of neutrons by a given isotope is not a simple function of its atomic number (for instance, the neutron attenuation coefficient of hydrogen is greater than that of lead). The technique therefore offers advantages over x-ray imaging when it is necessary to image hydrogen or certain other light nuclides, especially when they are surrounded by heavier material, for instance, the imaging of water transport in hydrogen fuel cells. The ease of imaging

hydrogen with neutrons also makes the technique useful for studying the structure of biological objects, but these applications have been explored less than mechanical ones. Most studies using neutron imaging to examine biological material have examined the movement of water through some sample, such as the absorption of water by wood (Lehmann et al., 1999, 2000, 2001, 2005; Niemz et al., 2002) or the movement of water inside or near roots (DeJesus et al., 2002; Okuni et al., 2001a,b).

In this study, neutron tomography was used for the structural analysis of dried corn kernels. One would expect most of the imaged hydrogen in these samples to be contained in starch (67.8–74.0%, dry weight basis) and water (7–23%, wet weight basis), as well as in some protein, fiber, fat and sugar (Watson, 2003). The goal of the study was to determine if it was possible to easily view anatomical features of corn kernels using neutron tomography, and if so, to compare different types of kernels to see if structural differences were apparent. Specifically, kernels of two different corn varieties were compared: VA35 and GT-MAS:gk. For each variety, kernels which had been inoculated with *Aspergillus flavus* were compared with uninfected controls. GT-MAS:gk is resistant to infection by *A. flavus*, whereas VA35 is susceptible. This provided a system with good controls for study by neutron tomography, since any effects of the fungus observed in the susceptible variety would be expected to be reduced or absent in the resistant variety.

Additionally, the *A. flavus*-inoculated corn kernel system was chosen in this study because *A. flavus* is a well-known and problematic fungus in agriculture. *A. flavus* infects corn and other crops throughout the U.S. and contaminates these crops with aflatoxins (Cleveland et al., 2003), which have been shown to be toxic and highly carcinogenic to humans and animals (Eaton and Groopman, 1994). Aflatoxins produced by *A. flavus* in our kernels were used as a marker to verify that the kernels had been infected. The mode of *A. flavus* infection in corn kernels has been studied (Brown et al., 1995) with the aim of developing strategies for preventing fungal infection of kernels and aflatoxin contamination. Neutron tomography could be a valuable non-destructive method for studying the internal processes of *A. flavus* infection and invasion of corn kernels, all of which are still not well understood.

## 2. Experimental

### 2.1. Inoculation of corn kernels with A. flavus

Two corn genotypes were planted in SRRC field plots on April 2, 2004: GT-MAS:gk, which possesses resistance to the fungus and aflatoxin contamination (Guo et al., 2001; Widstrom et al., 1987), and VA35, a susceptible genotype (Williams et al., 2005). Previously reported procedures were used for the preparation of *A. flavus* cultures and inoculum on potato dextrose agar (PDA), and for the inoculation of corn ears (Brown et al., 1991). Using sterile deionized water containing 0.01% Triton X-100, conidial spores were washed from the surface of the fungal mycelium growing on PDA. The conidial suspension was diluted to a number density of $5 \times 10^6 \, mL^{-1}$, as determined with a hemocytometer. Each

genotype was wound-inoculated in the field 7 days after self-pollination by injecting the mid ear at multiple locations with approximately 1 mL per injection, using a 50-mL syringe and a 12-gauge needle. Some ears were wounded with syringe needles without inoculum to serve as wounded-only controls. After the kernels reached maturity (about 35 days after pollination), healthy-looking intact kernels immediately adjacent to the inoculation sites were collected. Kernels removed from approximately the same region of uninoculated ears served as controls. This procedure resulted in four types of kernels for study: susceptible inoculated (hereafter $S_I$), susceptible control ($S_C$), resistant inoculated ($R_I$) and resistant control ($R_C$). Ten kernels of each type were removed from ears and dried for 4 days at 32 °C for further analysis by neutron tomography and determination of aflatoxin concentrations.

### 2.2. Neutron tomography

The first neutron radiography was performed on kernels on March 20, 2005 using thermal neutrons at the BT-6 imaging facility of the NIST Center for Neutron Research (Hussey et al., 2005). Ten kernels of each of the four types were supported in separate columns by aluminum foil, and all four columns were imaged at the same time (Fig. 2A). The bases of the aluminum foil columns were attached to aluminum tubing, with 3–4 kernels of each sample inside the tubing and the rest supported only by the foil. The columns were arranged parallel to, and equidistant from, the axis of rotation for tomography. Kernels were irradiated using the facility's 1-cm aperture, giving a neutron beam with a fluence rate of about $4.8 \times 10^6 \, cm^{-2} \, s^{-1}$ and an *L/D* ratio of about 600. A Li-doped ZnS scintillator screen (Applied Scintillation Technologies, Harlow, U.K.[2]) placed behind the kernels was photographed using a CCD camera, which was cooled to −40 °C. To avoid radiation damage, the camera was placed above the beam axis rather than directly behind the scintillator, and photographs of the scintillator were taken using a mirror. The imaging resolution of this configuration was limited by blooming of the scintillator to about 150 μm. For computed tomography, the kernels were imaged every 0.5° as they were rotated through 180°. At each imaging angle, two 50 s exposures were taken and averaged. To obtain normalized transmission radiographs, dark currents were subtracted from each of the raw exposures, which were then divided by a beam profile image. Finally, the software Octopus (Dierick et al., 2004) was used to reconstruct the 3D distribution of neutron attenuation coefficient in the kernels.

Additional tomography was performed on kernels on July 13, 2005, using a Varian Paxscan 2520 amorphous silicon flat panel detector with the high energy option (Hytec, Inc., Los Alamos, NM). This detector had somewhat lower pixel

---

[2] Certain trade names and company products are mentioned in the text or identified in an illustration in order to adequately specify the experimental procedure and equipment used. In no case does such identification imply recommendation or endorsement by the National Institute of Standards and Technology or the Agricultural Research Service, nor does it imply that the products are necessarily the best available for the purpose.

pitch than the CCD detector (127 μm rather than 50 μm), but was radiation-hard and could therefore be placed directly against the scintillator (Fig. 2B). This configuration avoids the need for optics and mirrors, and allows for increased light collection. Thus, exposure times could be reduced to just 1 s, from 50 s required by the CCD configuration. Using the AmSil detector, 10 new $S_I$ and $S_C$ kernels from the original batch of kernels were imaged; additional $R_I$ and $R_C$ kernels were not available for imaging. The 10 $S_I$ and $S_C$ kernels were supported along the sides of a single aluminum tube, rather than above separate tubes as before (Fig. 2B). They were then imaged every 0.5° as they were rotated through 180°. Ten 1-s exposures were taken and averaged at each angle. Octopus was again used for obtaining reconstructions.

In order to easily refer to unique kernel sets, they will be named in the rest of this paper by an abbreviation specifying the detector followed by an abbreviation specifying the kernel type. For instance, the set of susceptible inoculated ($S_I$) kernels imaged by the amorphous silicon detector (AmSil) will be referred to as AmSil-$S_I$. Altogether, reconstructions were obtained for six kernel sets: CCD-$S_C$, CCD-$S_I$, CCD-$R_C$, CCD-$R_I$, AmSil-$S_C$, and AmSil-$S_I$. To reference unique individual kernels, a kernel index number from 1 to 10 will be added to the set designation: for instance, CCD-$S_C$-$K_1$ for Kernel 1 of the CCD-$S_C$ set.

### 2.3. 3D reconstruction analysis

After obtaining reconstructions of the kernels, the software VGStudio (Volume Graphics, Heidelberg, Germany) was used to visualize the 3D image data. Reconstructed kernels were segmented (i.e., separated) so that each kernel could be manipulated in space (rotated, translated, etc.) and analyzed independently of others. Kernels were then arranged so that, as closely as possible, they were all in the same orientation, with the embryo side facing the viewer. A false-color scheme was applied to the 3D images to aid in visualizing the distribution of neutron attenuation coefficient within the kernels (see color bars, Figs. 3, 4 and 6); lighting was also applied in order to generate shadows, which helped highlight surface features. Finally, a sequence of images was generated in which material was incrementally "shaved" off the side of the kernels facing the viewer, so that layers at all depths through the kernels could be examined. This image sequence was generated for the 10 kernels of each of the kernel sets. The images were then examined for anatomical details, and to compare the sample types (e.g., $S_I$ vs. $S_C$) with each other.

When comparing sample types, a type of histogram analysis was used in addition to simple visual comparison of the slice sequences. A histogram showing the abundance of different neutron attenuation coefficients was generated for each individual kernel, by integrating the volume of each attenuation coefficient throughout the entire volume of the kernel. The distributions of attenuation coefficient for different sample types were then compared.

A few kernels from the AmSil-$S_I$ and AmSil-$S_C$ sets were also physically dissected after tomography was performed.

Kernels were first soaked in water for about 24 h, and then sliced into 0.5 mm sections using a razor. These raw slices were photographed, then stained for starch with iodine and photographed again. Finally, the correspondence between these physical slices and the slices reconstructed from tomography was examined.

### 2.4. Aflatoxin analysis

After tomography was performed, kernels imaged with the CCD detector (but not the amorphous silicon detector) were analyzed for their aflatoxin B1 content by a procedure similar to the one used in an earlier study (Brown et al., 1993). Each corn kernel was placed in a clear plastic polyethylene sample bag and pulverized with a hammer. Pulverized material was weighed and transferred into a 50 mL Erlenmeyer flask with a ground glass stopper containing 25 mL methylene chloride and shaken for 30 min at 1000 rpm on an orbital shaker (Lab-Line Instruments, Inc., Melrose Park, IL). Flask contents were decanted into a 50 mL beaker, and remaining residue in the flask was washed ($\sim 1$–$2$ mL, 3 times) with methylene chloride; this wash was also decanted into the 50 mL beaker. Beaker contents were dried passively in a chemical fume hood overnight. The following day, dried residue was solubilized in a small amount (1–2 mL, 3 times) of methylene chloride and transferred into a two dram glass vial and dried passively overnight. This material was then solubilized in 100–200 μL methanol and filtered by centrifugation at $15{,}996 \times g$ for 1 min in a 2 mL filter centrifuge tube (Costar, 0.45 μm pore size, nylon filter) for analysis by high performance liquid chromatography (HPLC).

HPLC for analysis of aflatoxin was conducted under conditions similar to those reported by Sobolev and Dorner (2002). A Nova-Pak $C_{18}$ column (150 × 3.9 mm; 4 μm) was used in a model 2690 separations module; peaks were detected using a model 2475 fluorescence detector, all from Waters Corporation, Milford, MA. Fluorescence detection sensitivity was enhanced using a photochemical reactor for postcolumn derivatization (PHRED system; Aura Industries, New York). The chromatography software Millennium (Waters) was utilized. HPLC was performed with a column temperature of 38 °C, a flow rate of 0.8 mL $min^{-1}$, an injection volume of 10 μL, a mobile phase of water/methanol/1-butanol (1400:720:15, v/v), and detector wavelengths of 365 nm (excitation) and 440 nm (emission). Thin layer chromatography (TLC) was also performed, using ether/methanol/water (96:3:1, v/v) and Si250F 20-$cm^2$ silica gel plates (J.T. Baker), as a confirmatory test for the presence of aflatoxin in the corn kernels (Brown et al., 1991).

## 3. Results

### 3.1. Identification of anatomical features

After performing neutron radiography and computed tomography, reconstructions of the kernels were examined for anatomical details (Fig. 1). The scutellum, endosperm, aleurone

**Tomographic Reconstruction**                                    **Anatomical Drawing**
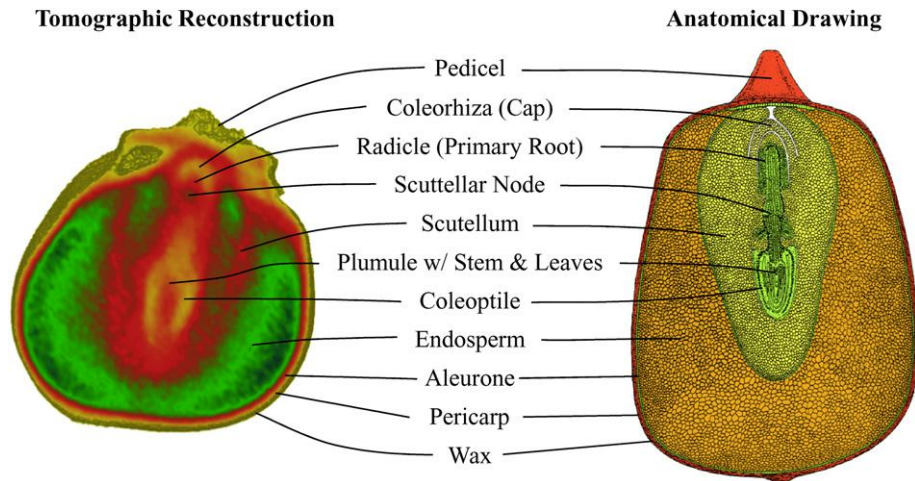


Fig. 1. Identification of anatomical features: many structures visible in the corn kernel reconstructions were identifiable as well-known anatomical features of corn kernels. The anatomical drawing is from a well-known research bulletin by Kiesselbach (1949), reproduced with the permission of the University of Nebraska-Lincoln.

and pericarp (layers) were clearly distinguishable. Identifiable structures were the pedicel, coleorhiza, radical, plumule, and coleoptile. The scutellar node was also tentatively identified.

To further examine the correspondence between reconstructed kernel structures and their direct physical structure, kernels of the AmSil-$S_I$ and AmSil-$S_C$ sets were sliced into sections with a razor. Photographs of these physical slices with and without iodine stain were compared to their corresponding reconstructed slices; this comparison is shown in Fig. 3 for the single kernel AmSil-$S_I$-$K_5$. In the unstained

physical slices (Fig. 3A), two distinct regions of the endosperm were visible: the horny endosperm, which was yellow and toward the outside of the kernel, and the floury endosperm, which was whiter and toward the center of the kernel (Watson, 2003). The scutellum was also clearly visible. Other visible features included a small "U"-shaped yellow endosperm region (probably a region of high-density endosperm) just below the scutellum (blue box), and embryo structures within the scutellum (white box). In the iodine-stained physical slices (Fig. 3C), the two layers of the endosperm stained equally and
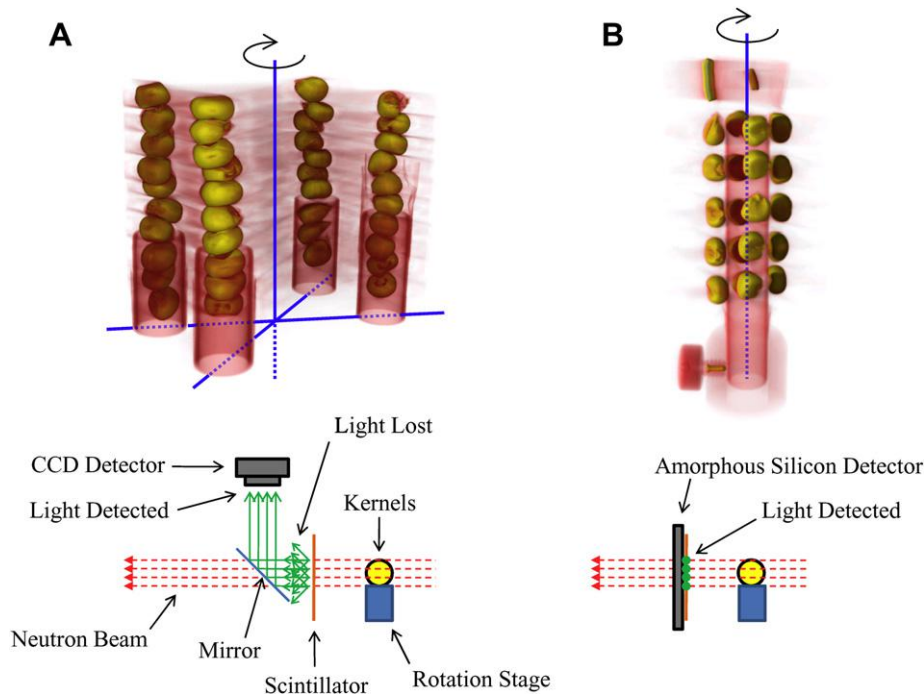


Fig. 2. Kernel imaging geometry and tomography schematic: complete tomographic reconstructions of the kernels show how they were arranged for radiography. Axes of rotation used for tomography are shown with vertical blue lines. Aluminum support tubing used to position the kernels is clearly visible (in red) in the reconstruction. Schematic diagrams below illustrate how tomography was performed using the CCD and AmSil detectors. Apparatus is viewed from the side, with the ground toward the bottom of the page.
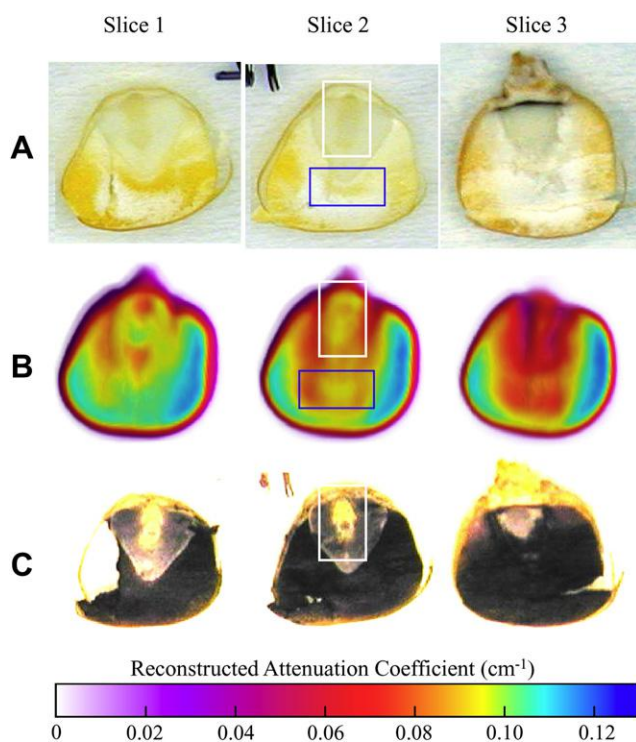
Fig. 3. Reconstructed vs. physical kernel slices: reconstructed corn kernel slices (B) of AmSil-$S_I$-$K_5$ were compared with stained (C) and unstained (A) physical slices of the same kernel. The colored bar at the bottom of the figure gives the neutron attenuation coefficients for the reconstructed slices in B.

were no longer distinguishable. However, the iodine stain highlighted the boundaries between the endosperm, scutellum, and embryo. The endosperm stained the most darkly for starch, while the scutellum stained somewhat less and the embryo stained very little.

The main structural correspondence observed was of the yellow horny endosperm in the unstained physical slices to the areas of higher neutron attenuation in the reconstructed slices. In Fig. 3, the yellow areas of the outer perimeter of the endosperm in (A), Columns 2–3 correspond very well with the blue, high neutron attenuation areas of (B), Columns 2–3. Conversely, the large, white floury endosperm region in (A) corresponds well with the large, red, low-attenuation area in (B); this is especially noticeable in Column 3. The small yellow "U"-shaped endosperm region enclosed by the blue box in (A) also compares well with the boxed region in (B), as do the embryo structures enclosed by white boxes.

### 3.2. Verification of A. flavus infection

When kernels surrounding the ear inoculation sites were destructively analyzed for aflatoxin (after tomography), only the CCD-$S_I$ kernels were found to contain detectable amounts of toxin (Fig. 4A), showing that *A. flavus* had infected these kernels. No aflatoxin was detected in the CCD-$R_I$ kernels, consistent with the reported resistance of GT-MAS:gk to *A. flavus* and aflatoxin contamination (Guo et al., 2001; Widstrom et al., 1987). Aflatoxin was also not detected in the controls, CCD-$S_C$

and CCD-$R_C$. These results confirmed that the kernels imaged with the CCD detector had been infected (or not) as expected, so that any observed effects in the reconstructions could be plausibly attributed to infection. Kernels imaged by the AmSil detector were not tested for aflatoxin, but were prepared by the same methods as those imaged by the CCD detector, and were almost certainly infected in the expected way.

### 3.3. Tomographic slice and histogram comparisons of different kernel treatments

After examining the anatomical details in the reconstructions, slices reconstructed from the inoculated kernel sets were compared to those reconstructed from the uninoculated controls (CCD-$S_I$ vs. CCD-$S_C$, CCD-$R_I$ vs. CCD-$R_C$, and AmSil-$S_I$ vs. AmSil-$S_C$). It should be noted that the aluminum tubing used to support the kernels caused an artificial reduction of $9.4 \pm 0.8\%$ (data not shown) in the reconstructed attenuation coefficients of kernels 8–10 in the CCD-$S_C$, CCD-$R_C$, and CCD-$R_I$ sets, and of kernels 7–10 in the CCD-$S_I$ set, which was probably due to beam hardening. These kernels were affected because they were fully enclosed by the aluminum support tubing, as can be seen in Fig. 2A. Because of this error, these kernels were not included in the analysis of the reconstructed slices. They were included in the histogram analysis (Fig. 5A and B), but with a correction for the 10% reduction in attenuation. The kernels of the AmSil-$S_I$ and AmSil-$S_C$ sets were unaffected since they were all placed in equivalent positions along the side of a single aluminum tube.

For all kernel sets, the histograms (Fig. 5) of neutron coefficient abundance shared a similar overall structure. All histograms had peaks in the very low-attenuation region (coefficients of 0–0.03 cm$^{-1}$) which merely corresponded to empty space in the reconstructions (the white to purple areas in Figs. 3, 4 and 6). The rest of the histogram (coefficients 0.03–0.13 cm$^{-1}$) corresponded to the bulk of the actual reconstructed kernels (the purple to blue areas in reconstructed slices). Thus, this was the region of interest when examining all of the histograms.

The most obvious differences between the CCD-$S_I$ and CCD-$S_C$ reconstruction slices (Fig. 4A) were the regions of low attenuation (purple to red, coefficients of 0.03–0.06 cm$^{-1}$) in the centers of the CCD-$S_I$ kernels, relative to the CCD-$S_C$ kernels. This effect was most pronounced in CCD-$S_I$-$K_1$ and $K_6$, but was also apparent in $K_2$ through $K_5$. By contrast, the kernels of the CCD-$S_C$ set appeared to have more material with medium attenuation (coefficients of 0.06–0.08 cm$^{-1}$) in their centers. The existence of this additional medium-attenuation material in the CCD-$S_C$ slices was supported by the histograms (Fig. 5A). Most of the CCD-$S_C$ histograms (red) had pronounced peaks in the medium-attenuation region (0.06–0.08 cm$^{-1}$). In the CCD-$S_I$ histograms (blue), however, no such peaks were present in the medium-attenuation region. The regions of low-attenuation material seen in the CCD-$S_I$ reconstructions were not reflected as clearly in the histograms, probably because they were masked by the integration of low-attenuation noise in the empty volume surrounding the
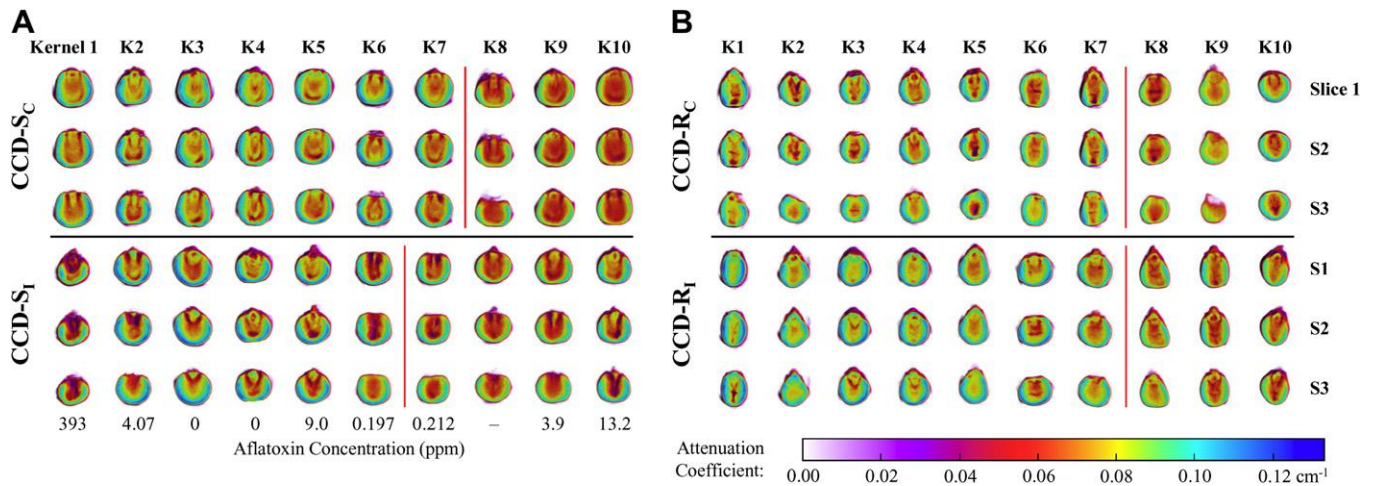
Fig. 4. Control vs. inoculated kernel reconstructions (CCD detector): reconstructed slices of the CCD-S$_C$, S$_I$, R$_C$ and R$_I$ kernel sets are compared. For each kernel, three slices from near the center of the kernel are shown. Kernels 8–10 of the CCD-S$_C$, R$_C$ and R$_I$ sets and kernels 7–10 of the CCD-S$_I$ set (set apart by vertical bars) appear to be redder (lower attenuation) in the center than the rest of the kernels; this effect is an artifact of the aluminum tubes (see Section 3 and Fig. 2A) and should be disregarded. Aflatoxin concentrations measured in each kernel are also shown; the maximum statistical error in these measurements is 5%. No aflatoxin was detected in any of the CCD-R kernels.
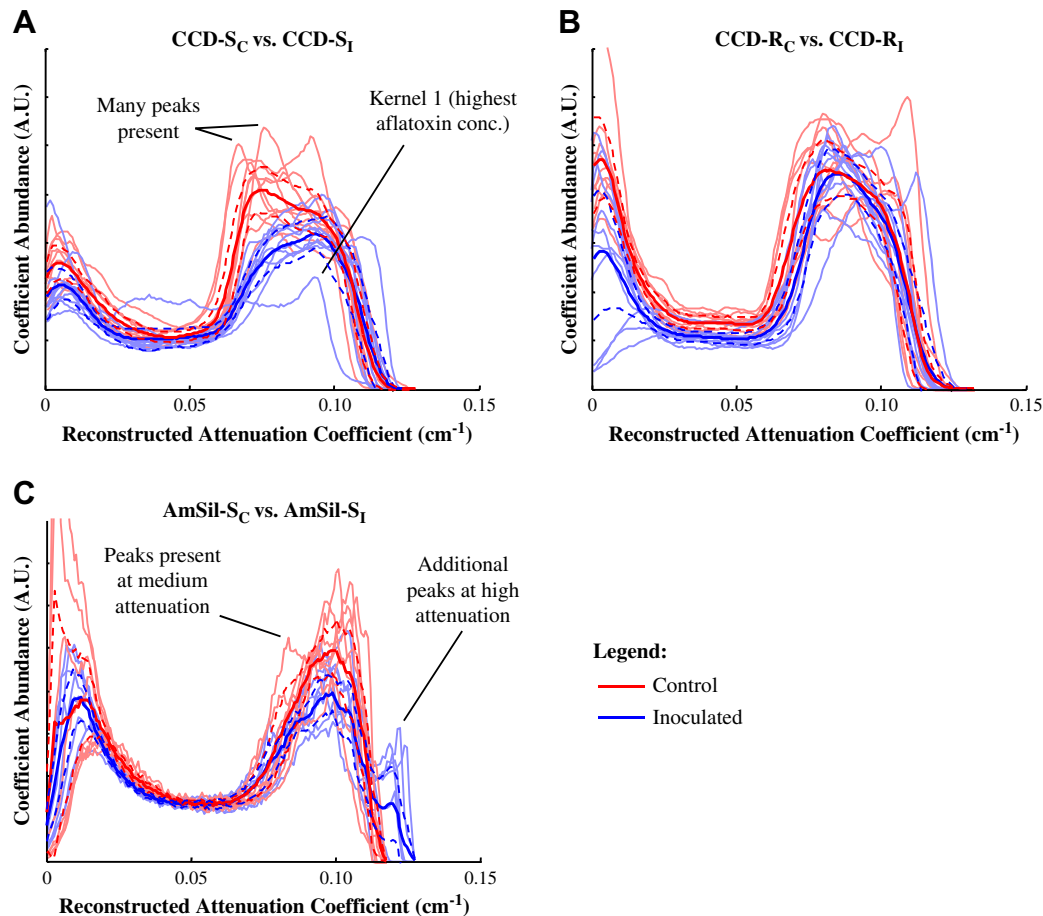


Fig. 5. Histograms of neutron attenuation coefficients: the abundance (in arbitrary units of volume) of different neutron attenuation coefficients in the kernel reconstructions is shown. Faint curves are the histograms of single kernels, and a bold curve is the average of all 10 single kernel histograms of a treatment. Bold dashed curves show the 95% CIs of the averaged histograms.
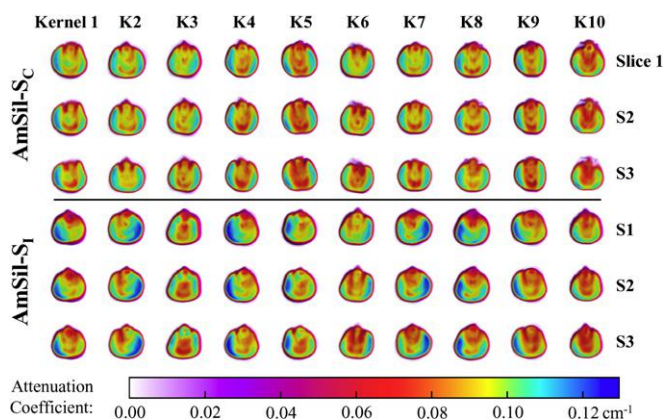
Fig. 6. Susceptible control vs. inoculated kernel reconstructions (AmSil detector): reconstructed slices of the AmSil-S_C and AmSil-S_I kernel sets are compared. The most obvious differences are the regions of high attenuation coefficients (deep blue, coefficients greater than 0.12) in the endosperms of the inoculated kernels. Aflatoxin concentration was not measured in AmSil kernels.

kernels. However, this increased volume of low-attenuation material can be seen clearly in the histogram for the notable kernel CCD-$S_I$-$K_1$. This kernel's histogram curve had a markedly different shape than the other CCD-$S_I$ curves. In particular, it appeared that much more of the kernel's volume consisted of low-attenuation ($0.03-0.06$ cm$^{-1}$) material. In Fig. 4A, it was apparent that this low-attenuation material was mostly present in the center (scutellum and embryo) of the kernel (see purple areas in the center of the Kernel 1 slices). This kernel also had the highest aflatoxin concentration by far (Fig. 4A, Kernel 1) of any of the inoculated kernels, confirming the presence of *A. flavus* infection.

Visually, there were no clear systematic differences between the CCD-$R_I$ and CCD-$R_C$ kernel tomographic slices (Fig. 4B), which was expected since these kernels were known to be resistant to infection by the fungus (Widstrom, 1987). Likewise, there were no apparent significant differences between the individual kernel histograms of the CCD-$R_I$ and CCD-$R_C$ kernel sets in Fig. 5B.

The clearest differences between the AmSil-$S_I$ and AmSil-$S_C$ reconstruction slices (Fig. 6) were the regions of high attenuation (coefficients greater than $0.12$ cm$^{-1}$) present in the endosperms of many of the AmSil-$S_I$ kernels (particularly: AmSil-$S_I$-$K_1$, $K_2$, $K_4$, $K_5$, and $K_7-K_9$) but none of the AmSil-$S_C$ kernels. The high attenuation regions seen in the AmSil-$S_I$ slices were consistent with the peaks at coefficients of about $0.12-0.13$ cm$^{-1}$ in the AmSil-$S_I$ histograms (Fig. 5C, blue). These peaks were not present in the AmSil-$S_C$ histograms (red), just as the high attenuation regions were not apparent in the AmSil-$S_C$ slices. Another difference was the smaller volume of material with coefficients of $0.08-0.12$ cm$^{-1}$ present in the AmSil-$S_I$ histograms relative to the AmSil-$S_C$ histograms. In the slices, the main structures comprised of these coefficients appeared to be embryo structures, near the center and top-center of the kernels.

## 4. Discussion

It is clear that many anatomical structures of the kernels were identifiable in the reconstructions. First, the structures seen in the reconstructions resembled known corn kernel structures, as shown in Fig. 1. Second, a correspondence was seen between structures in kernel reconstructions and structures in the physical slices of the same kernel, as shown in Fig. 3 for a single kernel. This comparison was particularly useful, since anatomical structures could be identified by traditional means in physical kernel slices, and then compared directly with structures in reconstructed slices of the very same kernel. The most noticeable features of the physical slices were two boundaries: one between the embryo and scutellum, and the other between the scutellum and endosperm. They were apparent in both the stained and unstained physical slices, but especially in the stained ones. These boundaries, however, were not the most noticeable features in the reconstructed slices. Instead, the boundary between the red and blue regions (see Fig. 3B, Column 3) was the most obvious feature. This boundary did not correspond to the boundary between embryo and scutellum, or between scutellum and endosperm, but to the boundary between the floury and horny endosperm layers. This boundary can be seen visually only in the unstained physical slices, and it is more subtle than the others; it is the boundary between the yellow edges and white interior of Fig. 3A, Column 3. It is known that upon drying, the floury endosperm develops empty spaces that fill with air. The horny endosperm, by contrast, has a stronger protein matrix, which causes its starch granules to be compressed without forming cavities (Watson, 2003). These air-filled cavities in the floury endosperm are a possible cause of its low neutron attenuation relative to the horny endosperm.

Since it was found that anatomical structures of kernels could be identified, the next goal of the study was to see if changes could be distinguished in these structures between kernels of different types. When comparing the kernel sets for differences, a useful technique was to examine the histograms in Fig. 5 for ranges of significant difference in attenuation coefficient abundance, then to determine which kernel structures in the reconstructions in Figs. 4 and 6 were comprised of those attenuation coefficients. This technique was effective because the histograms and reconstructed slices are, in a sense, complementary to each other. The histograms allow examination of the data of an entire kernel, but with no spatial information; whereas the slices allow one to see the exact spatial distribution of attenuation coefficient, but only in small sections of the kernel. If correspondences are then observed between effects in the average histograms and effects in the individual slices, it is evidence that the effects seen in the individual slices may be significant throughout the kernel volume.

As described in Section 3, there was a peak in coefficient abundance over the medium-attenuation range of the CCD-$S_C$ histogram average (Fig. 5A, red), as compared to the coefficient abundance for the same range of the CCD-$S_I$ histogram average (blue). This peak seemed to correspond to the additional medium-attenuation material seen near the scutellum

in the CCD-$S_C$ reconstructions (Fig. 4A); the CCD-$S_I$ set, by contrast, appeared to have lower attenuation near the scutellum in the reconstructions. The kernel that appeared to be the most infected in Fig. 4A was CCD-$S_I$-$K_1$, which was also the kernel with the highest aflatoxin content. The individual histogram of this kernel, shown in Fig. 5A, appeared to be very different from the histograms of the other inoculated kernels. However, it can be understood as an extreme example of the differences between the inoculated and control histogram averages. In the medium-attenuation (0.06–0.08 cm$^{-1}$) range, the coefficient abundance in the CCD-$S_I$ histogram average was significantly decreased compared to the control. In the medium-high attenuation (0.08–0.11 cm$^{-1}$) range, the CCD-$S_I$ histogram average was not reduced as much, which is why it had its maximum in this range. The CCD-$S_I$-$K_1$ histogram in Fig. 5A was an extension of this pattern: the attenuation coefficient abundance in the medium range was much lower than in the control histograms; but there was a sharp peak in the high attenuation range where the coefficient abundance did not decrease as much. In the low-attenuation range (0.03–0.06 cm$^{-1}$), the coefficient abundance in the CCD-$S_I$-$K_1$ histogram was actually higher than that of the controls, because of the large volume of kernel material with significantly decreased attenuation.

A possible explanation for the observed pattern of change between the CCD-$S_C$ and CCD-$S_I$ histograms is that the fungus had degraded material in the embryos and scutella of the inoculated kernels. This degradation could decrease the attenuation coefficient of the material by releasing bound hydrogen as water (e.g., by metabolizing starch), which would be eliminated during kernel drying and thus decrease the material's hydrogen density. Fungal degradation could also have increased the permeability of the scutellum to allow more complete drying, which would also have reduced the hydrogen density. The scutella of the CCD-$S_C$ kernels can be seen in Fig. 4A to be comprised mostly of medium-attenuation (orange to yellow) material, which is the material that decreased most in abundance in the CCD-$S_I$ histograms. The abundance of higher-attenuation material did not decrease as much in the CCD-$S_I$ set. This higher-attenuation material is found mostly in the endosperms of the kernels, and its abundance would not be decreased as much if the fungus were attacking primarily the scutella. Finally, in Fig. 4A, the observed effects on kernel CCD-$S_C$-$K_1$ can again be understood as a logical extreme of this pattern of fungal invasion. The scutellum of this kernel contained a large volume of material with low attenuation, even when compared to some of the other inoculated kernels; and especially when compared to the controls. The endosperm, however, still contained some higher-attenuation material. Preferential fungal invasion of the embryo and scutellum, and lesser invasion of the endosperm, is consistent with previous findings. Brown et al. (1995) studied the modes of invasion of *A. flavus* in several lines of corn using *A. flavus* transformed with a reporter gene (*Escherichia coli* β-glucuronidase) that rendered the fungus detectable in the kernel. They reported that the embryo and scutellum appeared to be "the favored substrate for the fungus."

While there were very significant differences between the average histograms of the CCD-$S_C$ and CCD-$S_I$ sets (Fig. 5A), the average histograms of the CCD-$R_C$ and CCD-$R_I$ sets (Fig. 5B) were very similar (in fact, above 0.08 cm$^{-1}$, they were virtually identical). There is a stark contrast between A and B of Fig. 5; this contrast is the most convincing piece of evidence that differences can be observed between the inoculated and control kernels using neutron tomography. It is exactly the result one would have expected: since the kernels in B were resistant to infection by *A. flavus*, major differences were not found between the infected and control kernel sets as they were in A. In addition, no obvious systematic differences were visually apparent between the slices of the CCD-$R_C$ and CCD-$R_I$ sets (Fig. 4B).

When the AmSil-$S_C$ and AmSil-$S_I$ histograms were compared (Fig. 5C), the differences observed were not the same as those observed between the CCD-$S_C$ and CCD-$S_I$ sets. The AmSil-$S_I$ kernels contained less material with medium-high attenuation (0.08–0.12 cm$^{-1}$) than the AmSil-$S_C$ kernels, but their histograms had additional peaks in the high attenuation (0.12–0.13 cm$^{-1}$) range. The AmSil-$S_C$ kernels contained virtually no material with coefficients in this high attenuation range. When the CCD-$S_C$ and CCD-$S_I$ sets were compared, the inoculated kernels again had less medium-attenuation (0.06–0.08 cm$^{-1}$) material than the controls, but a comparable amount of medium-high attenuation (0.08–0.12 cm$^{-1}$) material. The CCD-$S_I$ kernel histograms did not have the additional peaks at 0.12–0.13 cm$^{-1}$ seen in the AmSil-$S_I$ histograms.

When the reconstructed slices of the AmSil-$S_C$ and AmSil-$S_I$ kernels were compared (Fig. 6), it was clear that the high attenuation material observed in the AmSil-$S_I$ kernel histograms was mostly localized to the endosperm of the kernels (see deep blue areas in the AmSil-$S_I$ slices). The visual details in the AmSil-$S_I$ kernel slices were also somewhat less uniform than in the AmSil-$S_C$ slices. By simple visual appearance, the features of the AmSil-$S_C$ slices could be described as follows (from the outside to the inside of a kernel slice): a light-blue endosperm region on the left and right sides of the kernel, followed by a red-orange "U"-shaped "track", followed by a yellow-green oval-shaped region, which often contained a red "dot" at the tip of the kernel and a red "V" near the exact center of the kernel. This appearance was quite consistent across all of the AmSil-$S_C$ slices. Across the AmSil-$S_I$ slices, however, there was more variation. The deep blue (high attenuation) regions of the AmSil-$S_I$ slices were not distributed the same way in different kernels: they tended to fall on different sides of the endosperm (i.e., left or right), and sometimes would also encroach upon the center of the kernels (see, i.e., AmSil-$S_I$-$K_2$ and $K_7$).

In principle, the AmSil-$S_C$ vs. AmSil-$S_I$ comparison should not have differed from the CCD-$S_C$ vs. CCD-$S_I$ comparison as described above. The treatments being compared were the same ($S_C$ vs. $S_I$), so the same types of differences should have been observed between control and inoculated kernels. However, there are several possible explanations for this discrepancy. First, the comparison was performed between different kernel sets, which had been harvested at the same

time but imaged on different dates. The AmSil kernels were imaged nearly 4 months after the CCD kernels, and it is suspected that they absorbed moisture during this time (they were not stored in an environment with carefully controlled humidity). The major structural difference between the AmSil and CCD comparisons was the appearance of the high attenuation regions in the endosperms of the AmSil-$S_I$ kernels (the deep blue areas in the reconstructed slices). It is not known for certain what caused these regions to appear, but hydrogen in absorbed water could certainly have caused areas of significantly increased neutron attenuation to appear, consistent with what was observed. In this situation, it is conceivable that the AmSil-$S_I$ kernels acquired more water than the AmSil-$S_C$ kernels because the fungus had compromised their structure, possibly allowing more moisture to enter. It should be noted that even though differences between the AmSil-$S_I$ and $S_C$ kernels appeared in the endosperm, the fungal damage could actually have been to the embryo and scutellum, as with the CCD kernels. It could be that damage to the embryo, scutellum or pedicel allowed more moisture to enter, which then collected in the endosperm, causing changes to appear there. However, this was not determined conclusively. Changes to the concentrations of any of the hydrogen-bearing components of the kernels could have been responsible for the observed differences between the AmSil and the CCD kernels.

A second possible explanation for the structural differences between the CCD and AmSil comparisons is the differing arrangements of the kernels used when performing tomography. However, this does not seem likely. The difference in geometry would not have caused structural differences to appear only in the AmSil-$S_I$ kernels, but not the AmSil-$S_C$ kernels as well. Finally, a third explanation is that the change in detector from CCD to AmSil caused the structural differences. This too seems unlikely, for the same reason: it should not have caused differences to appear only in the AmSil-$S_I$ kernels.

In any case, it should be noted that the AmSil-$S_C$ and AmSil-$S_I$ kernels were stored together at all times, imaged at the same time as each other, and positioned in a symmetrical arrangement during tomography. Therefore, regardless of the differences from the CCD comparison, it was still reasonable to conclude that the observed differences between AmSil-$S_C$ and AmSil-$S_I$ were caused by fungal infection.

## Acknowledgements

## References

Brown, R.L., Cleveland, T.E., Payne, G.A., Woloshuk, C.P., Campbell, K.W., White, D.G., 1995. Determination of resistance to aflatoxin production in maize kernels and detection of fungal colonization using an *Aspergillus flavus* transformant expressing *Escherichia coli* β-glucuronidase. Phytopathology 85, 983–989.

Brown, R.L., Cotty, P.J., Cleveland, T.E., 1991. Reduction in aflatoxin content of maize by atoxigenic strains of *Aspergillus flavus*. Journal of Food Protection 54 (8), 623–629.

Brown, R.L., Cotty, P.J., Cleveland, T.E., Widstrom, N.W., 1993. Living maize embryo influences accumulation of aflatoxin in maize kernels. Journal of Food Protection 56, 967–971.

Cleveland, T.E., Dowd, P.F., Desjardins, A.E., Bhatnagar, D., Cotty, P.J., 2003. Pre-harvest prevention of mycotoxins and mycotoxigenic fungi in crops. Pest Management Science 59, 629–642.

Dierick, M., Masschaele, B., Van Hoorebeke, L., 2004. Octopus, a fast and user-friendly tomographic reconstruction package developed in LabView. Measurement Science and Technology 15, 1366–1370.

DeJesus, S., Crispim, V., Brandão, L., 2002. The use of neutron radiography in agriculture to improve the food quality. Cellular and Molecular Biology (Noisy-Le-Grand) 48 (7), 819–821.

Eaton, D.L., Groopman, J.D., 1994. The Toxicology of Aflatoxins: Human Health, Veterinary, and Agricultural Significance. Academic Press Inc., San Diego, CA, p. 544.

Guo, B.Z., Li, R.G., Widstrom, N.W., Lynch, R.E., Cleveland, T.E., 2001. Genetic variation within maize population GT-MAS:gk and the relationship with resistance to *Aspergillus flavus* and aflatoxin production. Theoretical and Applied Genetics 103, 533–539.

Hussey, D.S., Jacobson, D.L., Arif, M., Huffman, P.R., Williams, R.E., Cook, J.C., 2005. New neutron imaging facility at the NIST. Nuclear Instruments and Methods in Physics Research Section A 542 (1–3), 9–15.

Kiesselbach, T.A., 1949. The structure and reproduction of corn. Nebraska Agricultural Experiment Station Research Bulletin 161, 1–96.

Lehmann, E., Hartmann, S., Wyer, P., 2005. Neutron radiography as visualization and quantification method for conservation measures of wood firmness enhancement. Nuclear Instruments and Methods in Physics Research Section A 542 (1–3), 87–94.

Lehmann, E.H., Vontobel, P., Niemz, P., 1999. Investigation of Moisture Distribution in Wooden Structures by Neutron Radiography. PSI Annual Report Annex VI, p. 53.

Lehmann, E.H., Vontobel, P., Niemz, P., Haller, P., 2000. The method of neutron radiography and its use for wood properties analysis. In: Proceedings of the International Conference on Wood and Wood Fibre Composites, Stuttgart, Germany.

Lehmann, E.H., Vontobel, P., Scherrer, P., Niemz, P., 2001. Application of neutron radiography as method in the analysis of wood. Holz als Roh- und Werkstoff 59 (6), 463–471.

Niemz, P., Lehmann, E.H., Vontobel, P., Haller, P., Hanschke, S., 2002. Investigations using neutron radiography for evaluations of moisture ingress into corner connections of wood. Holz als Roh- und Werkstoff 60 (2), 118–126.

Okuni, Y., Furukawa, J., Matsubayashi, M., Nakanishi, T., 2001a. Water accumulation in the vicinity of a soybean root imbedded in soil revealed by neutron beam. Analytical Sciences 17, 1499–1501.

Okuni, Y., Furukawa, J., Matsubayashi, M., Nakanishi, T., 2001b. Water movement in the vicinity of a seedling root with aluminum treatment by neutron beam imaging. Radioisotopes 50 (6), 270–274.

Sobolev, V.B., Dorner, J.W., 2002. Cleanup procedure for determination of aflatoxins in major agricultural commodities by liquid chromatography. Journal of AOAC International 85, 642–645.

Watson, S.A., 2003. Description, development, structure, and composition of the corn kernel. In: White, P.J., Johnson, L.A. (Eds.), Corn: Chemistry and Technology, second ed. American Association of Cereal Chemists Inc., St. Paul, MN, pp. 69–106.

Widstrom, N.W., McMillian, W.W., Wilson, D., 1987. Segregation for resistance to aflatoxin contamination among seeds on an ear of hybrid maize. Crop Science 27, 961–963.

Williams, W.P., Windham, G.L., Buckley, P.M., 2005. Enhancing maize with resistance to *Aspergillus flavus* infection and aflatoxin contamination. In: Abbas, H. (Ed.), Aflatoxin and Food Safety. Taylor & Francis, New York, pp. 379–374.